Draft version May 9, 2019
Typeset using LaTeX **modern** style in AASTeX62

High-Resolution Multi-Epoch Astrometry of Water Fountain IRAS 16552-3050
University of New Mexico Honors Thesis

Patrick Latimer
Advisor: Ylva M. Pihlström

ABSTRACT

In the transition between the Asymptotic Giant Branch and the Planetary Nebula phases of stellar evolution lies the elusive class of objects known as Water Fountains (WFs). WFs exhibit high-velocity H_2O masers, likely tracing stellar jets as they carve structure into the surrounding dust. Only about a third of WFs possess an optical counterpart, and matches between the 15 confirmed WFs and the Gaia catalog yielded only 5 parallaxes, each with a large error. We present six epochs of Very Long Baseline Array (VLBA) data of WF IRAS 16552−3050. There is a strong, bipolar distribution, with two distinct groups of masers separated by ≈ 90 mas, spanning ≈ 210 km s^{-1} in velocity. The groups are expanding with an outflow velocity of ≈ 1.5 mas yr^{-1}, implying a dynamical age for the jet of ≈ 60 yr. No evidence of precession is found, and we suggest that the masers trace bow shocks.

1. INTRODUCTION

1.1. *Water Fountains and PrePlanetary Nebulae*

When an intermediate mass (0.8 - 8 $M_\odot$) star runs out of hydrogen to burn at its core, it expands to hundreds of times its main sequence size, burning heavier elements as it nears death. This stage of stellar evolution is known as the Asymptotic Giant Branch (AGB). AGB stars have slow, strong stellar winds, losing mass at a prodigious rate of up to 10^{-4} solar masses per year (Desmurs 2012). These winds create a large circumstellar envelope (CSE) of dust and gas, surrounding the star and obscuring it. Once the stellar core has fused all its Helium, and if it is not hot enough to fuse Carbon, the outer layers separate, leaving the core as a a compact, hot object known as a white dwarf. The white dwarf radiates intensely to ionize the surrounding gas, forming a planetary nebula (PN). The evolutionary steps that form the often bipolar and point-symmetric morphologies of PNe are not clear. The shift from a spherically symmetric AGB star to a more complex PN is notoriously difficult to observe, due both to the obscuration from the CSE and the very short lifetime of the transition

(estimated to be only in the hundreds of years). Objects in this stage are known as preplanetary nebulae (PPNe). [1]

The circumstellar envelope of AGB stars is home to some rather interesting chemistry. The range of elements and temperatures in the slowly expanding dust shell gives rise, most helpfully, to maser emission. The accurate positions and velocities of masers allows study of the gas dynamics in the CSE. In oxygen-rich stars, most commonly SiO, H_2O, and OH appear in concentric shells around the late AGB star and imply a stable slow outflow in the outer region traced by H_2O and OH. When the star begins the transition into a PN, these masers disappear sequentially from the inside out, giving little indication of the dynamics of the central regions of PPNe. However, some PPNe show water masers that have an abnormally large velocity range, leading them to be dubbed "Water Fountains" (WFs). Generally, the maser emission is clustered in two groups which are believed to trace high-velocity bipolar jets slamming into the surrounding CSE. This bipolar distribution with highly doppler shifted groups is exemplified in Fig. 1, in the case of IRAS 19190+1102. WFs were discovered when the prototypical example IRAS 16342-3814 was observed by Likkel & Morris (1988) to have an unprecedentedly high velocity range of 259 km s^{-1}. Since then, few additional WFs have been confirmed bringing the total count to only 15 (Gómez et. al. 2017). The low number of confirmed objects is in part due to their exceptionally short lifetimes, with dynamical ages estimated to be on average 100 years (Imai 2007). WFs are also difficult to discover and confirm, first requiring spectral-line surveys of late-type AGB stars likely to have H_2O emission, and interferometric followup of sources with large velocities to make sure the emission is from a single source.

Stellar jets likely provide the answer to the question of how PN morphologies come to be. Any theory of PPN dynamics must explain the presence of bipolar, multipolar, and point-symmetric morphologies in PNe, as well as explain the advent of such aspherical structures in the circumstellar envelope. A model for jet-assisted PN formation comes from Sahai & Trauger (1998), which proposed jets or collimated fast winds (CFWs) as the primary mechanism for symmetry breaking. The CFWs occur in the late AGB phase, and carve out the CSE, achieving complex patterns due to a precessing rotation axis or multidirectionality. The jets are likely episodic and rotating, in order to achieve point symmetry witnessed in a number of PNe (Sahai et. al. 2011). Magnetohydrodynamical models have been applied to the theory, and support it, though it remains unclear what stellar conditions are required to achieve instabilities leading to CFWs. Strong magnetic fields are thought to play a large part

[1] A note on nomenclature: when PNe were discovered, astronomers noted that they had resolvable disks, similar to planets. Thus these objects came to be known as Planetary Nebulae, despite having nothing to do with planets. To make matters worse, the field studying the formation of PNe began to use the term Proto-Planetary Nebula, which is awfully similar to Proto-Planetary Disk, the dusty disk surrounding a young star that eventually will become a planetary system. In hopes to slightly mitigate the confusion, some PPN researchers have begun to use the term preplanetary Nebula instead (Sahai, Contreras et. al. 2005), a convention this paper will follow.

in the collimation of jets, and a binary companion is thought necessary for jets to precess (Balick & Frank 2002).

The slow wind of the CSE and the jets occur before the star collapses into a white dwarf, merely setting the stage for the nebula. Coincident with the collapse, the star emits a very hot, isotropic fast wind, which fills the imprint left by the CFWs. This wind becomes the optically emitting portion of the PN (Sahai & Trauger 1998). After this event, the young PN gains even more structure with the continuation of fast collimated emission, interaction with the interstellar medium, and the passage of photoionization fronts (Sahai et. al. 2011). These processes are well understood, as mature PNe are easily observable optically. Thus the challenge remains in constraining the dynamics that produce young PNe. Water Fountains provide a valuable tool, tracing the very jets thought to create structure in PPNe. They may also provide a way to estimate a distance, as the water masers are sufficiently bright and compact to allow for Very Long Baseline Interferometry (VLBI) parallax measurements to be performed. An accurate distance estimate will enable much more exact physical parameters of the source to be calculated.

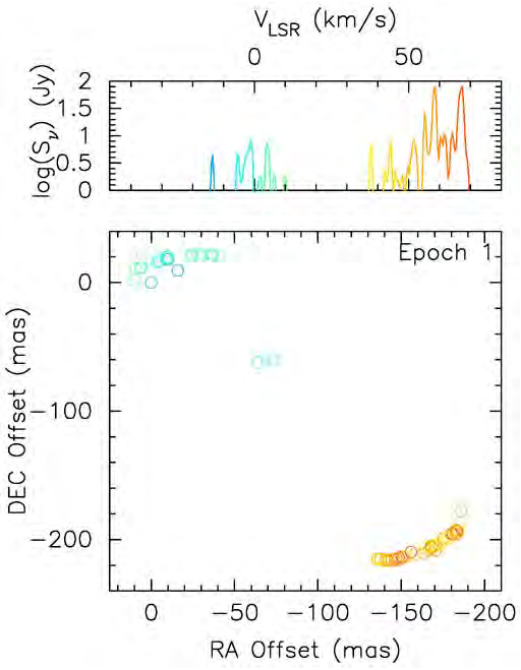

Figure 1. Maser positions and spectrum from Day et. al. (2010) Top: Maser strength as a function of doppler shifted velocity. Bottom: Maser distribution on the sky in Right Ascension and Declination. Note the small scale, spanning just over 200 milliarcseconds on a side.

VLBI is a relevant and necessary tool in the pursuit of WF distances. Though recent observations from the Gaia telescope have provided distances to 1.3 billion sources (Gaia Collaboration 2018), optical astrometry is inaccurate at best in the case of late AGB stars, due to extreme obscuration by dust. Of the 15 confirmed WFs listed in Gómez et. al. (2017), only five had counterparts in the Gaia catalog with attempts at parallax determination, shown in Table 1. As can be noted in the Table, all five sources have very large error in the listed Gaia parallaxes, leading to distance uncertainties. Masers provide a point source close to the central star with which to perform accurate parallax measurements. In this thesis we describe VLBI observation of water masers in the PPNe IRAS 16552−3050, to determine the environment and dynamics of these masers, as well as eventually derive a parallax distance.

IRAS Name	Alternate Name	Gaia Counterpart	Parallax [mas]	Parallax Error [mas]
15103−5754	GLMP 405	Y	0.0551	0.9159
15445−5449	OH 326.50.4	-	-	-
16342−3814	OH 344.1+5.8	Y	-	-
16552−3050	GLMP 498	-	-	-
17291−2147		Y	-1.4869	0.4602
18043−2116	OH 9.10.4	-	-	-
18113−2503	PM 1221	Y	0.0907	0.0597
18139−1816	OH 12.80.9	-	-	-
18286−0959	OH 21.800.13	-	-	-
18450−0148	W43A	-	-	-
18455+0448		Y	0.2182	0.1950
18460−0151	OH 31.00.2	-	-	-
18596+0315	OH 37.10.8	-	-	-
19134+2131		Y	2.3674	1.0162
19190+1102	PM 1298	-	-	-

Table 1. All Confirmed Water Fountain Sources from Gómez et. al. (2017), including Gaia matches and parallaxes (Gaia Collaboration 2018).

2. IRAS 16552-3050

IRAS 16552-3050 (hereafter IRAS 16552) was confirmed as a WF by Suárez et. al. (2008), with Very Large Array (VLA) observations made in 2006. They observed two groups of masers in a bipolar distribution separated by ≈ 80 mas at a position angle of $\approx 44°$. The masers featured a velocity difference between red and blueshifted components of ≈ 170 km s^{-1}, and were distributed almost perpendicular to the separation axis. This led the authors to posit a rapidly precessing/rotating bipolar jet as the cause of the maser emission. Like many other WFs, a visible or near-IR counterpart was not found, suggesting that WFs have thicker envelopes than other late AGB stars. This implies that they are relatively high-mass ($\gtrsim$ 4-5 $M_\odot$) (Suárez et. al. 2008).

3. OBSERVATIONS AND DATA CALIBRATION

Observations of IRAS 16552−3050 were performed using the VLBA, for six epochs between May 26, 2012 and May 14, 2013 (Table 2). The frequency setup was centered on the 22.235 GHz H_2O transition, and to cover the full velocity range of the known masers four single polarization IFs of 8 MHz each were used, each with 1024 spectral channels. The total velocity coverage was from -144 to $+234$ km s^{-1}, with a channel separation of 0.1 km s^{-1}.

As antennas used for VLBI span continents, we must be careful to include rigorous calibration for the different environments. Comparing the relative phase of incoming waves gives us positional information for our target, so it is vital to correct for phase errors between signals arriving at the different antennas. These phase errors include

Table 2. Observation details, used for positional error calculation

Epoch	Observation Date	Beam Size [arcsec]	Position Angle [degrees]
A	May 26, 2012	0.00095 x 0.00025	-5.56
B	July 30, 2012	0.00147 x 0.00030	-13.26
C	November 3, 2012	0.00101 x 0.00027	-7.05
D	December 30, 2012	0.00164 x 0.00037	10.86
E	March 4, 2013	0.00102 x 0.00028	-5.36
F	May 14, 2013	0.00164 x 0.00030	-13.64

a variety of errors in the delay model, but are dominated by phase errors introduced by the atmosphere. At 22 GHz the phase may vary on a timescale of 1-2 minutes, and the observations were performed in a phase-referencing mode, nodding between the calibrator J1650−2943 and target with a cycle time of 1.5 min. The data was calibrated using the AIPS package, following standard procedures for VLBI spectral line data. This included bandpass calibration using J2005+7752, and fringe-fitting for residual rates and delays using the phase calibrator J1650−2943. The solutions for the phase calibrator were interpolated to the target source.

After the initial calibration, bright maser features were located in the field-of-view. An iterative self-calibration and imaging procedure was used to improve the signal-to-noise ratio, hence absolute positions of the phase centers were lost. This procedure allows weaker features to be detected, and accurate relative positions between the maser features are obtained. The cubes have a typical 1σ rms noise of 27.5 mJy/channel. This calibration is needed to determine the full structure of the maser emission, both in velocity as well as in spatial coordinates.

Once a good, consistent maser is identified in all epochs, further calibration can take place in order to retain the absolute positions. This can be done by calculating phase corrections from the selected maser feature, and apply those to the calibrator instead. This is a process called reverse phase-referencing, in which the apparent shift of the calibrator is used to established the abolute motion across the sky for the masers. This type of calibration is needed for parallax calculation, and this work is still in progress (see also Sect. 5.2).

4. RESULTS AND DISCUSSION

4.1. *Maser Feature Positions*

The data were analyzed using AIPS, initially using spectral data to identify the peak channels of each maser. Care was taken to separate real emission from noise, leftover sidelobes and radio frequency interference. In their peak channel, masers were fitted with elliptical gaussians, which provided position and intensity for each feature. Positional uncertanties were calculated using the formula $\Delta\theta_i = (0.54\,\theta_{FWHM,i})/(S/N)$ where $\theta_{FWHM,i}$ is the FWHM of the synthesized beam in the i direction (Pihlström

et. al. 2018). The positional and flux information was then processed using custom python scripts.

The masers are arranged in two distinct groups, one with redshifted velocities around 100 km/s, and one with blueshifted velocities around −70 km/s. The maser spectrum is shown in Fig. 2. The redshifted group is consistently brighter and features more maser components than the blueshifted group. Though there is variability in the indidual masers between epochs, the redshifted group maintain a similar shape throughout, shown in Fig. 3. The positional errors are on average 0.016 mas, and are small in relation to the spatial distance between individual maser features.

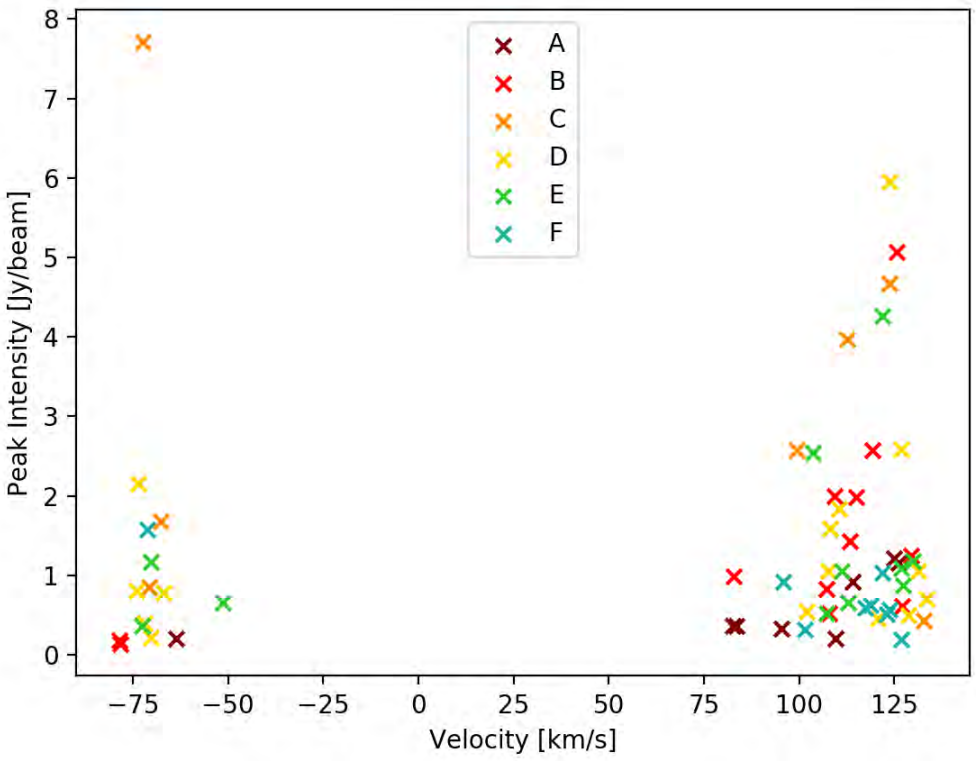

Figure 2. Intensity/velocity distribution of maser peaks in every epoch.

Though the central column of red masers is of particular interest for multi-epoch dynamics as it is relatively constant, some epochs exhibited less consistent extended structure (see Appendix). One interesting pattern is the sporadic existence of masers with an East-West distribution. Whereas the consistent North-South structure led Suárez et. al. (2008) to suggest that the jet is rapidly precessing, the addition of E-W structure may instead indicate the presence of a bow shock. This structure is commonly found with jets, and traces an arc like the shock waves that come off of the bow of a boat in water. The detection of such a symmetrical structure suggests that previous observations could only see half the shock. In addition, the position angle

Figure 3. Offset positions of individual maser features in the redshifted (top) and blueshifted (bottom) groups of masers, relative to the brightest group maser in each epoch. This maser was used for self-calibration, and is indicated by the black plus sign. Size of the marker corresponds to relative strength of the maser component, and marker color is mapped to LSR velocity.

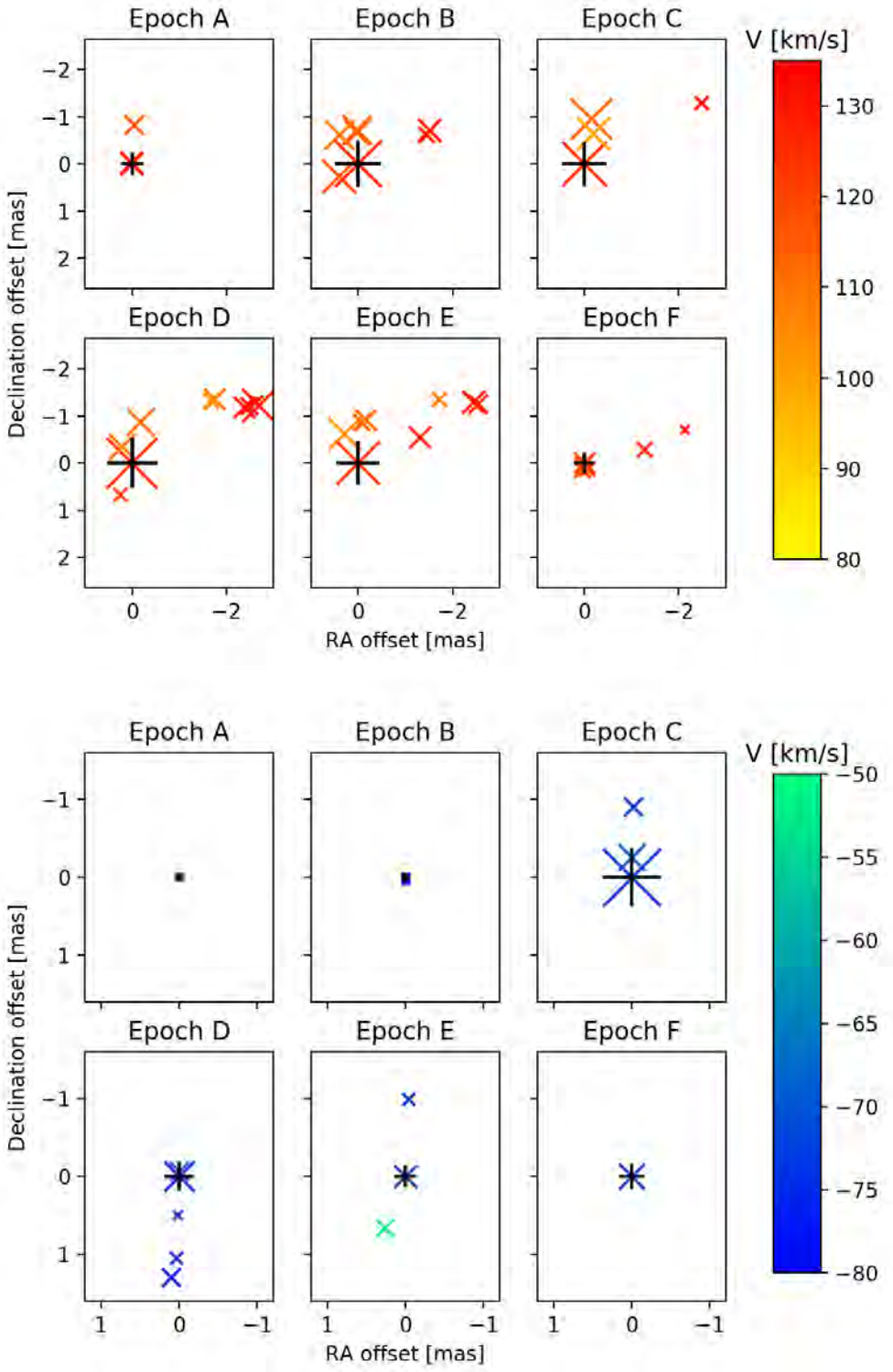

of the separation axis remained fairly constant at $\approx 44°$ both throughout the 2012 observations, consistent with the 2006 VLA observations. This implies that either precession is too small in amplitude to be recognized by our observations, or it is taking place on larger timescales than we are sensitive to. Of the WFs with observed precessions, the periods tend to be around 50 yr, with small angular amplitudes of $\lesssim 5°$(Sahai, Le Mignant et. al. 2005).

4.2. *Internal system kinematics*

To determine the outflow velocity of the system, we measured the relative separation between the two maser groups as a function of time. The separation between the blueshifted and redshifted groups is in the neighborhood of 90 mas. The redshifted group covers a velocity range of approximately 80 to 140 km/s (relative to the mean motion of the solar neighborhood, known as the Local Standard of Rest or LSR). The masers in the blueshifted velocity group are generally much weaker than those in the redshifted group, and only hosts 1-5 individual masers, covering a velocity range of -50 to -80 km/s. In order to calculate an angular separation between groups that is accurate and consistent between epochs, The brightest maser in each group was used. In the redshifted velocity group, the brightest maser maintained a central position relative to the overal persistent structure. The blueshifted masers are close and few enough that the brightest maser has an essentially equivalent position to that of the group.

The angular separation equation for two points on the sky with coordinates (α_1, δ_1) and (α_2, δ_2) is given by

$$\theta = arccos[sin(\delta_1) * sin(\delta_2) + cos(\delta_1)cos(\delta_2)sin(\alpha_1 - \alpha_2)] \tag{1}$$

To find the error, we used the general error calculation formula for a multivariable function $\theta(x_i)$ with variable errors $\{dx_i\}$:

$$d\theta = \sqrt{\sum_i \left(\frac{\partial\theta}{\partial x_i} dx_i\right)^2} \tag{2}$$

The group separation for each epoch is shown in Fig. 4. There is a slight outward trend, of ≈ 1.5 mas yr^{-1}. The 1σ separation errors are mostly quite small, with the exception of epoch B, which was due to a significantly lower signal and higher noise than in the other epochs (see Appendix). It should be noted that the observations of Suárez et. al. (2008) six years prior found an angular separation of ≈ 80 mas, which is fully consistent with the small expansion velocity we observed.

It is typical to assume a constant expansion velocity and calculate a dynamical age for systems such as this. This is useful in comparing similar objects at least on the order of magnitude level, though it may not be very physical to assume constant expansion. Given an expansion velocity of 1.5 mas yr^{-1} and a separation of ≈ 90

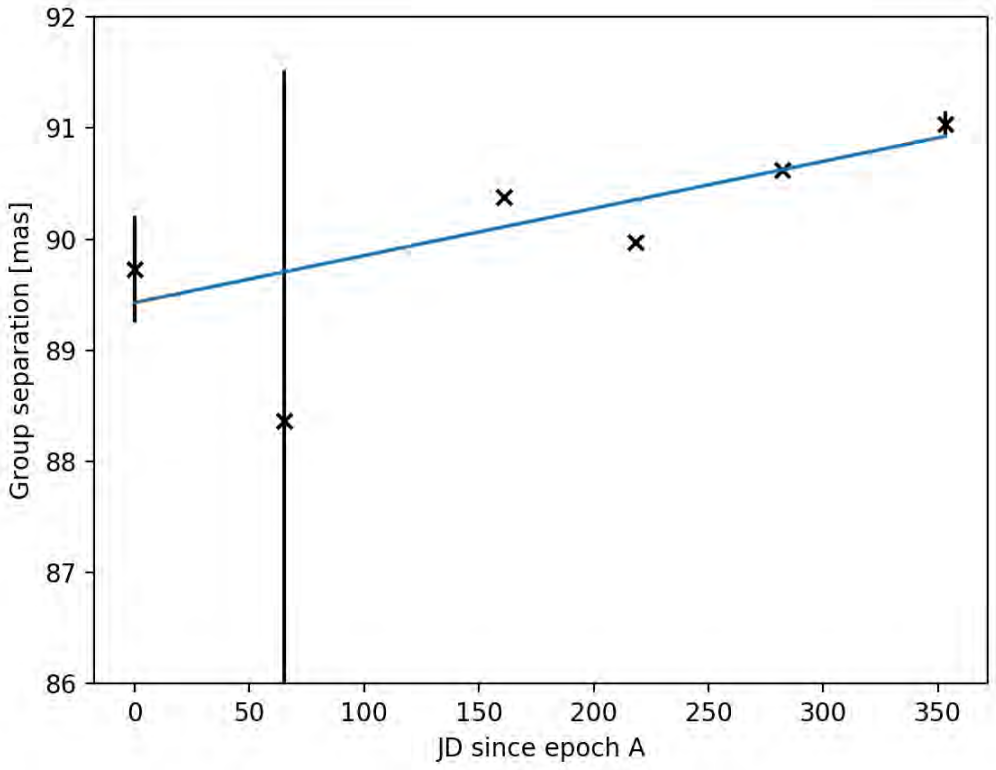

Figure 4. Angular separation between maser groups by as a function of Julian Date of each epoch. The error bars represent 1σ errors. The blue solid line is a linear least squares fit of 1.5 mas/yr.

mas, the dynamical age for the jet is estimated to be ≈ 60 yr, similar to that of other WFs (Desmurs 2012). This dynamical age calculation may not correspond to the actual age of the jet, not just because it assumes constant proper motion. It is unclear exactly how water masers relate to the jet as a whole. For instance, the jet could be significantly larger than the region suggested by the maser groups, which are there because H_2O is more abundant in the inner regions of the CSE (Yung et. al. 2017). However, as bow shocks would likely exist near the tip of a jet, their existence may indicate that the water masers are truly tracing the jet's end. Whatever the physical significance of the age, it is notable that WFs all have similarly short dynamical ages under 100 yr.

5. CONCLUSIONS AND FUTURE WORK

5.1. *Summary*

Water Fountains present an opportunity to study the dynamics of objects during the transition from spherical symmetry in the AGB phase to more complex symmetries as a Planetary Nebula. With 6 epochs of high-resolution VLBA data, We have confirmed

IRAS 16552−3050 to be a WF with a typical bipolar distribution. As in other WFs, it is theorized that the masers trace stellar jets.

- Matching the 15 previously confirmed WFs with the Gaia catalog yielded only 5 parallaxes, all with large error. This emphasizes the need for VLBI not only to characterize maser dynamics, but to derive accurate distances to WFs.
- We have identified two distinct groups of maser emission, separated spatially by $\approx$ 90 mas with a position angle of $\approx 44°$. These groups have a velocity distribution spanning $\approx$ 210 km s^{-1}, with a redshifted group at around 115 $\pm$ 13 km s^{-1}, and a weaker blueshifted group at around -70 $\pm$ 6 km s^{-1} (Fig. 2).
- The redshifted maser group exhibited a persistent North-South structure, as well as more inconsistent masers in the West and South directions. This implies that the masers exist in bow shocks formed as jets plow through the dust of the CSE. No evidence of jet precession was found.
- By comparing the brightest masers in each velocity group, we have derived an expansion velocity for the system of $\approx$ 1.5 mas yr^{-1}. This is consistent with the previous observations in 2006 by Suárez et. al. (2008), who measured a group separation of $\approx$ 80 mas. The expansion velocity gives jet a dynamical age of $\approx$ 60 years.

5.2. *Absolute Motion*

Eventually, we aim to measure the parallax distance to our target. Generally, absolute positions are found by applying phase corrections from the phase calibrator, but it was too weak for us to perform the full phase calibration. We instead intend to apply the method of reverse phase calibration, measuring the shift of the calibrator source when applying the phase corrections from the target. The phase calibrator used was J1650−2943. In order to perform precise parallax and proper motion measurements, we used the brightest maser in each group and corrected the position along the axis of separation for an expansion of 1.5 mas yr^{-1}. These positions were then corrected for the offset observed for the calibrator. The resulting absolute positions followed a motion that is not well fit by a sinusoid with a period of a year. The data are quite noisy, making it difficult to glean an accurate position for the calibrator, and at the writing of this thesis the absolute positions are not considered reliable. Further recalibration of the data will better constrain the absolute motions of the maser components. The resulting parallax and proper motion measurements will be described in a future publication.

5.3. *Followup Observations 2019*

In March 2019, another epoch of VLBA observations was performed in conjunction with the UNM Radio Astronomy course. The observation setup exactly matched that

described in this thesis. Comparison will provide valuable insight into the long-term dynamics of IRAS 16552−3050. It will also further constrain the expansion velocity and proper motion. Results will be described in a future publication.

REFERENCES

Balick, Bruce; Frank, Adam 2002 ARA&A40, 439

Day, F. M.; Pihlström, Y. M.; Claussen, M. J.; Sahai, R. 2010 ApJ, 713, 986

Desmurs, J. F. 2012, IAUS, 287, 217

Gaia Collaboration et. al. 2018, A&A, 616, A1

Gómez, J. F.; Suárez, O.; Rizzo, J. R.; Uscango, L.; Walsh, A.; Miranda, L. F.; Bendjoya, P. 2017, MNRAS, 468, 2081

Imai, H. 2007 IAUS, 242, 279

Likkel, L.; Morris, M. 1988 ApJ, 329, 914

Pihlström, Y. M.; Sjouwerman, L. O.; Claussen, M. J; Morris, M. R.; Rich, R. M.; van Langevelde, H. J.; Quiroga-Nuñez, L. H. 2018, ApJ, 868, 72

Sahai, R.; Contreras, C. S., Morris, M. 2005, ApJ, 620, 948

Sahai, R.; Le Mignant, D.; Sánchez Contreras, C.; Campbell, R. D.; Chaffee, F. H. 2005 , 622, 53

Sahai, R., Trauger, J. T. 1998 AJ, 116, 1357

Sahai, R., Morris, M. R., Villar, G. G. 2011 AJ, 141, 134

Suárez, O., Gómez, J. F., Miranda, L. F. 2008, ApJ, 689, 430

Yung, Bosco H. K.; Nakashima, Jun-ichi; Hsia, Chih-Hao; Imai, Hiroshi 2017, MNRAS, 465, 4482

APPENDIX

A. MASER DISTRIBUTIONS BY EPOCH

The individual maser information in each epoch are listed and plotted below. Position offsets are listed in reference to the brightest red maser in each epoch. The positional errors correspond to the process discussed in section 4.2, using the rms listed and the beam sizes listed in Table 2.

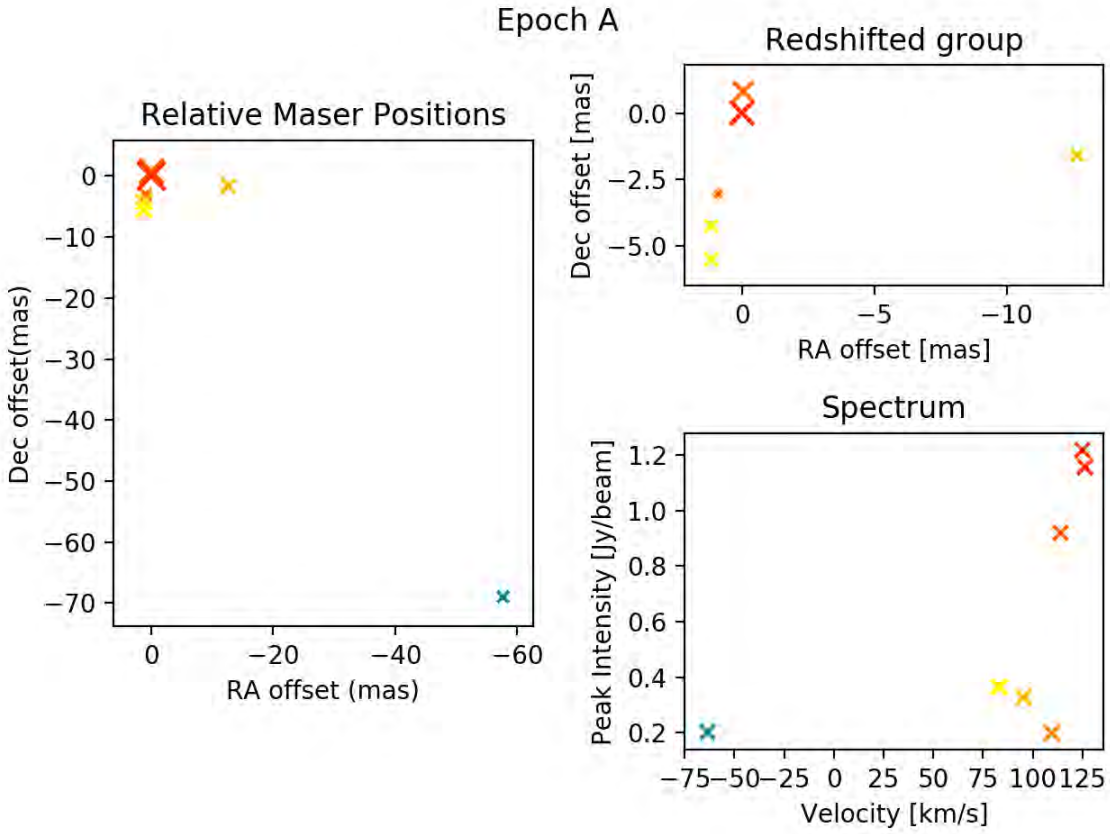

LSR Velocity [km s^{-1}]	Peak Intensity [Jy]	Channel rms [Jy]	RA offset [mas]	Dec offset [mas]	RA error [μas]	Dec error [μas]
125.0	1.2182E+00	2.826e-02	0.0	-0.0	2.7	10.1
114.0	9.1976E-01	2.588E-02	-0.048	0.824	3.7	13.9
126.2	1.1574E+00	2.586e-02	0.009	0.026	2.5	9.3
83.5	3.6510E-01	2.480E-02	1.161	-4.247	7.8	29.8
109.6	1.9869E-01	2.510E-02	0.899	-3.045	14.8	56.2
82.6	3.6609E-01	2.416E-02	1.166	-5.522	7.2	27.2
95.3	3.2691E-01	2.593E-02	-12.667	-1.584	11.1	42.2
-63.6	2.0410E-01	2.672e-02	-57.557	-68.837	16.0	60.8

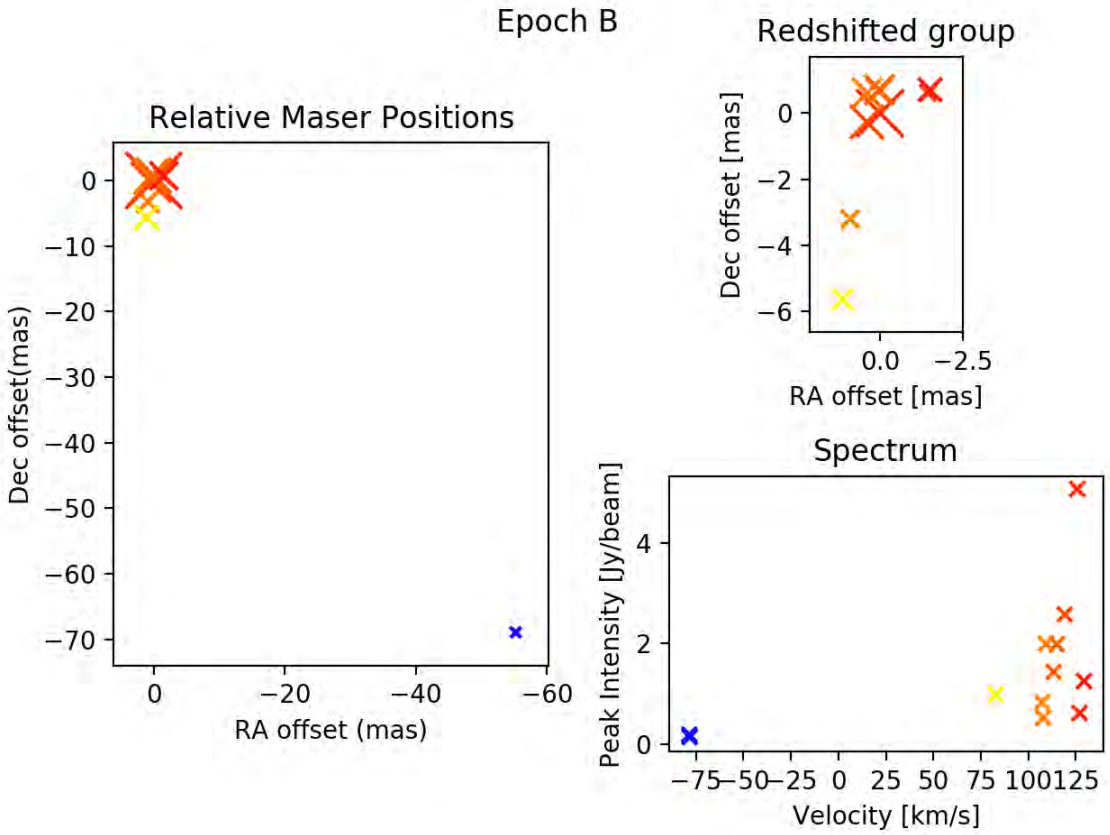

LSR Velocity [km s^{-1}]	Peak Intensity [Jy]	Channel rms [Jy]	RA offset [mas]	Dec offset [mas]	RA error [μas]	Dec error [μas]
107.8	5.2080E-01	2.516e-02	0.912	-3.196	5.7	27.9
107.2	8.2588E-01	2.790e-02	0.9	-3.214	5.0	24.5
82.9	9.8193E-01	2.783e-02	1.142	-5.645	4.2	20.6
125.7	5.0662E+00	3.874e-02	0.0	-0.0	0.9	4.4
119.2	2.5718E+00	3.141e-02	0.405	-0.265	1.7	8.6
114.9	1.9813E+00	3.153E-02	0.025	0.718	2.7	13.1
109.3	1.9910E+00	3.189E-02	0.396	0.612	2.1	10.2
113.3	1.4328E+00	3.108E-02	0.027	0.664	2.5	12.3
129.3	1.2498E+00	3.142E-02	-1.515	0.712	4.0	19.8
127.0	6.1399E-01	2.770E-02	-1.452	0.614	7.8	38.1
-78.3	1.3728E-01	2.853e-02	-55.313	-68.987	27.3	133.7
-78.5	1.8276E-01	3.293E-02	-55.28	-68.941	32.0	157.0

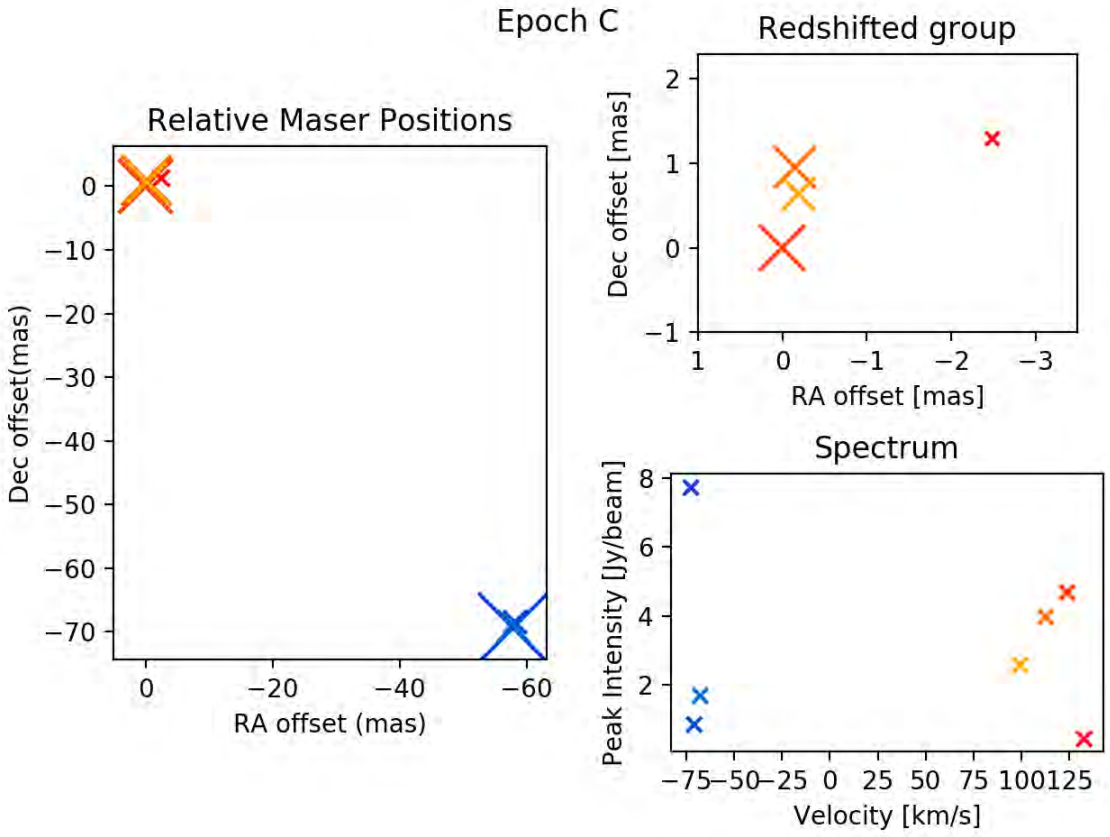

LSR Velocity [km s^{-1}]	Peak Intensity [Jy]	Channel rms [Jy]	RA offset [mas]	Dec offset [mas]	RA error [μas]	Dec error [μas]
123.7	4.6751E+00	2.809E-02	0.0	-0.0	0.9	3.4
132.6	4.3010E-01	1.966E-02	-2.489	1.291	6.4	24.0
112.6	3.9638E+00	2.931E-02	-0.151	0.952	1.3	4.7
99.3	2.5765E+00	3.428E-02	-0.191	0.638	1.3	4.7
-72.4	7.7117E+00	3.542E-02	-57.881	-69.415	0.6	2.3
-67.6	1.6832E+00	2.468E-02	-57.916	-69.159	2.0	7.5
-70.7	8.4711E-01	2.606E-02	-58.161	-68.505	4.2	15.7

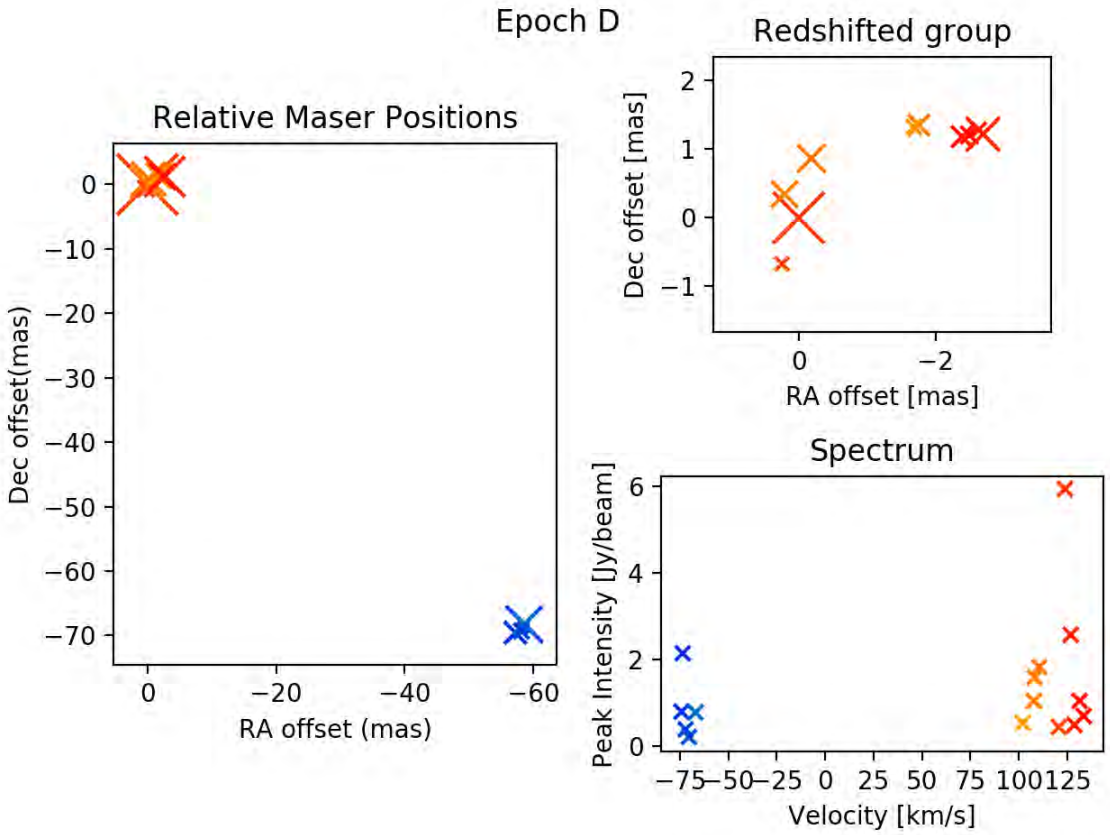

LSR Velocity [km s^{-1}]	Peak Intensity [Jy]	Channel rms [Jy]	RA offset [mas]	Dec offset [mas]	RA error [μas]	Dec error [μas]
123.7	5.9463E+00	4.071E-02	0.0	0.0	1.3	5.9
108.1	1.5905E+00	3.758E-02	0.208	0.344	3.0	13.3
110.5	1.8319E+00	3.171E-02	-0.184	0.868	3.5	15.7
120.6	4.4858E-01	2.607E-02	0.248	-0.673	8.1	35.7
107.7	1.0505E+00	3.403E-02	-1.756	1.352	5.4	23.8
102.0	5.4177E-01	2.665E-02	-1.68	1.324	5.7	25.5
126.7	2.5796E+00	3.662E-02	-2.692	1.219	2.5	11.0
133.4	7.0064E-01	2.851E-02	-2.494	1.208	8.5	37.6
131.3	1.0504E+00	3.061E-02	-2.386	1.183	5.8	25.6
128.6	4.9779E-01	2.586E-02	-2.633	1.286	10.0	44.3
-74.1	8.0161E-01	2.937E-02	-57.2	-69.575	7.6	33.6
-73.5	2.1498E+00	3.222E-02	-58.588	-68.282	3.1	14.0
-66.9	7.8530E-01	2.608E-02	-58.597	-68.213	6.6	29.3
-70.3	2.1755E-01	2.632E-02	-58.351	-68.777	16.2	71.8
-72.0	3.9341E-01	2.552E-02	-58.149	-69.329	9.7	43.0

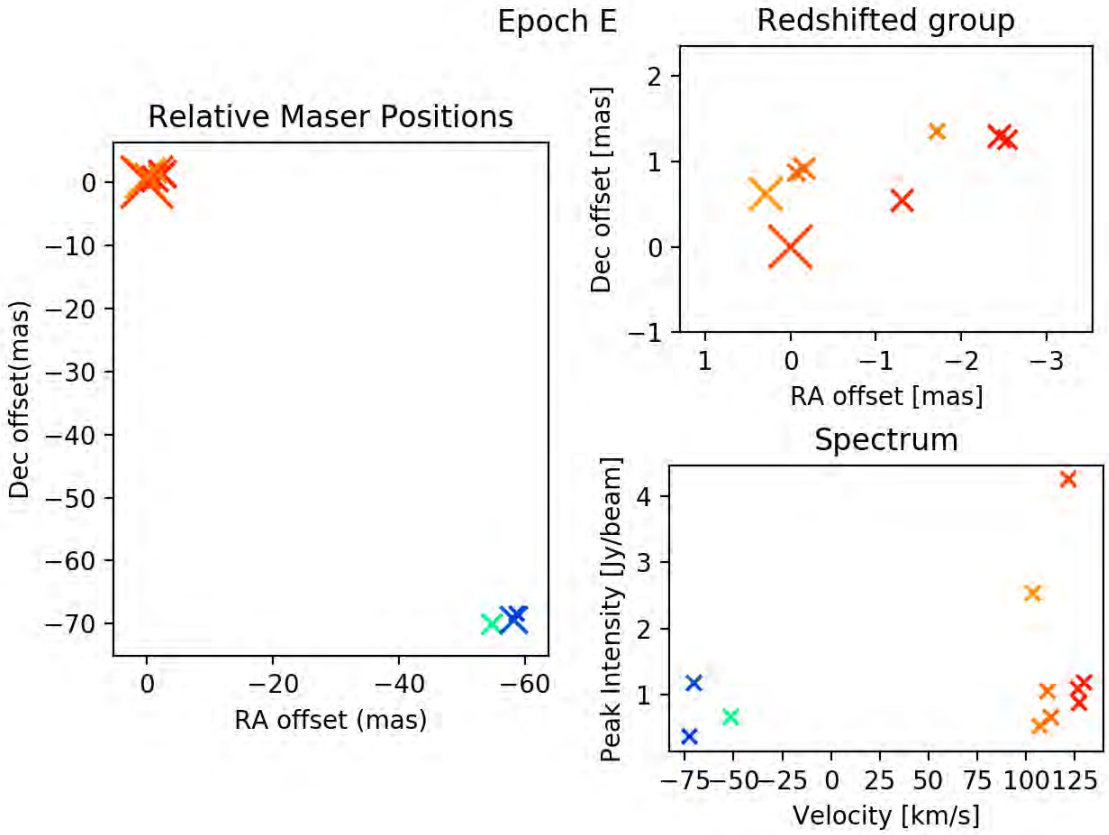

LSR Velocity [km s^{-1}]	Peak Intensity [Jy]	Channel rms [Jy]	RA offset [mas]	Dec offset [mas]	RA error [μas]	Dec error [μas]
129.8	1.1823E+00	2.022E-02	-2.448	1.293	2.6	9.6
126.7	1.0881E+00	1.955E-02	-1.311	0.543	2.9	10.4
127.3	8.7391E-01	1.894E-02	-2.544	1.253	2.7	9.9
107.1	5.2404E-01	1.866E-02	-1.72	1.35	5.8	21.3
103.5	2.5358E+00	3.164E-02	0.29	0.62	1.4	5.2
121.8	4.2622E+00	2.408E-02	0.0	0.0	0.6	2.3
111.1	1.0536E+00	1.892E-02	-0.163	0.915	3.0	10.8
112.8	6.5409E-01	1.796E-02	-0.072	0.867	4.3	15.6
-51.4	6.5914E-01	1.673E-02	-54.822	-70.059	3.7	13.4
-70.3	1.1729E+00	2.066E-02	-58.272	-69.404	3.1	11.2
-72.6	3.6549E-01	1.729E-02	-58.706	-68.409	7.5	27.3

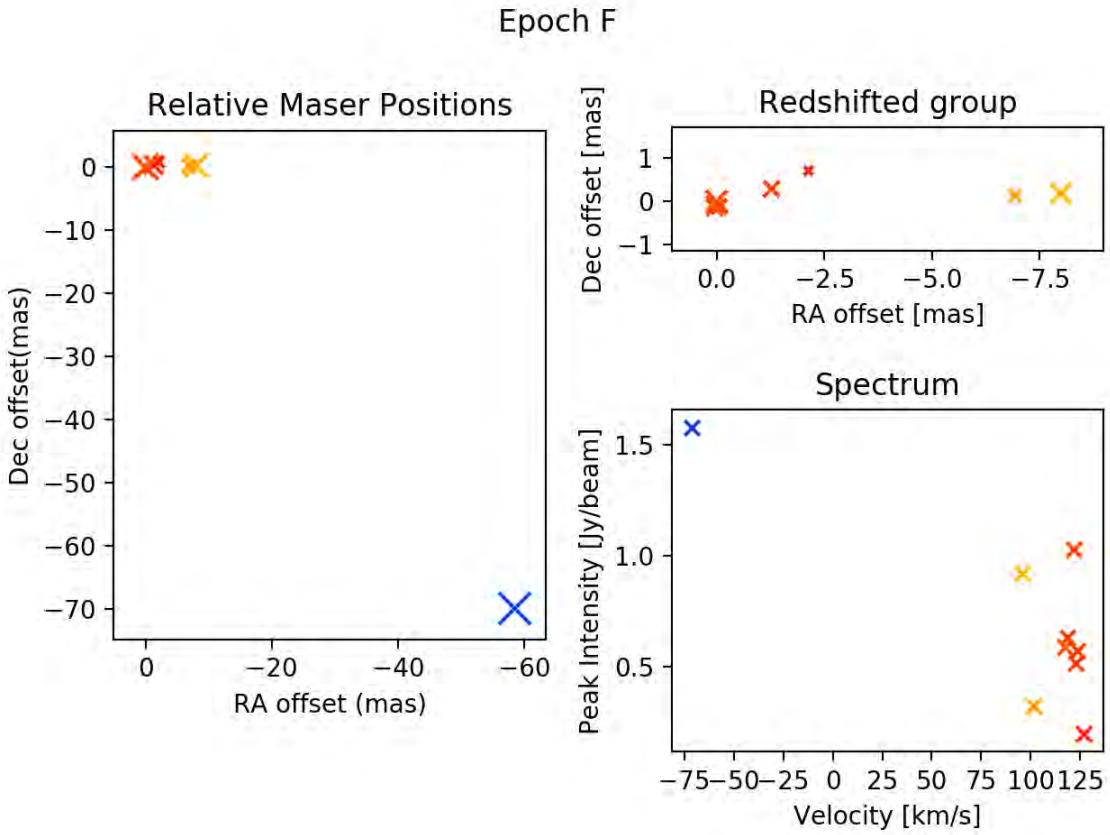

LSR Velocity [km s^{-1}]	Peak Intensity [Jy]	Channel rms [Jy]	RA offset [mas]	Dec offset [mas]	RA error [μas]	Dec error [μas]
95.9	9.1704E-01	2.952E-02	-7.984	0.177	5.4	29.4
123.7	5.6835E-01	2.661E-02	-1.276	0.284	6.5	35.8
101.6	3.1872E-01	2.430E-02	-6.923	0.126	11.7	64.1
126.9	1.9266E-01	2.008E-02	-2.13	0.707	12.1	66.0
122.9	5.1193E-01	2.557E-02	-0.066	-0.125	6.6	36.3
121.8	1.0263E+00	2.802E-02	0.0	-0.0	4.4	23.8
118.7	6.2855E-01	2.647E-02	0.045	-0.145	6.3	34.4
117.4	5.8525E-01	2.843E-02	0.039	-0.055	6.6	36.0
-71.2	1.5803E+00	3.993E-02	-58.465	-69.786	3.4	18.8